JGR Oceans

RESEARCH ARTICLE

10.1029/2022JC018686

Key Points:

- Transport rates of mixed sand with bimodal distribution are similar to those of well-sorted coarse sand
- Plug flow formation depends on the particle size distribution and occurs for the bimodal distribution
- Phase lags in sediment entrainment and sediment settling are important for predicting net transport rates

Correspondence to:

Y. Rafati,
yashar@udel.edu

Citation:

Rafati, Y., Hsu, T.-J., Calantoni, J., & Puleo, J. (2022). Entrainment and transport of well-sorted and mixed sediment under wave motion. *Journal of Geophysical Research: Oceans*, *127*, e2022JC018686. https://doi.org/10.1029/2022JC018686

Received 28 MAR 2022
Accepted 21 JUL 2022

Author Contributions:

Conceptualization: Yashar Rafati, Tian-Jian Hsu, Joseph Calantoni, Jack Puleo
Funding acquisition: Tian-Jian Hsu, Jack Puleo
Investigation: Yashar Rafati
Methodology: Yashar Rafati, Tian-Jian Hsu, Joseph Calantoni
Supervision: Tian-Jian Hsu
Validation: Yashar Rafati
Visualization: Yashar Rafati
Writing – original draft: Yashar Rafati, Tian-Jian Hsu
Writing – review & editing: Joseph Calantoni, Jack Puleo

Entrainment and Transport of Well-Sorted and Mixed Sediment Under Wave Motion

Yashar Rafati[1,2], Tian-Jian Hsu[3], Joseph Calantoni[4], and Jack Puleo[3]

[1]Environmental Hydrology and Design Group, Environmental Science Associates (ESA), Oakland, CA, USA, [2]Formerly at Center for Applied Coastal Research, Department of Civil and Environmental Engineering, University of Delaware, Newark, DE, USA, [3]Center for Applied Coastal Research, Department of Civil and Environmental Engineering, University of Delaware, Newark, DE, USA, [4]Ocean Sciences Division, U.S. Naval Research Laboratory, Stennis Space Center, MS, USA

Abstract Entrainment and suspension of sediment particles with the size distribution similar to a range of natural sands were simulated with a focus on the vertical size sorting and transport dynamics in response to different wave conditions. The simulations were performed using a two-phase Eulerian-Lagrangian model by combining the LIGGGHTS discrete element method solver for sediment and SedFoam solver for the fluid phase. The model was first validated for a range of sand grain sizes from 0.21 to 0.97 mm having well-sorted and mixed (bimodal) size distributions using laboratory oscillatory flow data. Three sediment bed configurations were studied under a wide range of velocity-skewed waves with different wave intensity and skewness. It was found that the bimodal distribution having only 30% of coarse fraction and 70% of medium fraction responds similar to a well-sorted coarse sand configuration. Sediment fluxes of the bimodal distribution were slightly higher than those of well-sorted coarse sand because of the pronounced inverse grading in the bimodal distribution. Furthermore, for the bimodal distribution the medium fraction acted as a relatively smooth foundation underneath the coarse fraction which facilitated the mobilization of the coarser particles. Under high energy wave conditions, the smoothing feature was exacerbated and further caused the formation of plug flow where a thick layer of intense sediment flux was observed. Model results also showed that under high skewness waves, phase-lag effect occurred in well-sorted medium sand which caused lower net onshore sediment transport rates but the effect was significantly reduced for mixed sediments.

Plain Language Summary Sediment transport driven by shoreward propagating waves depends on the sediment particle size. Generally, coarse particles (greater than 0.5 mm diameter) respond directly to the wave motion due to being entrained and transported near the bed with faster settling whereas medium particles (smaller than 0.3 mm diameter) do not respond directly to the flow field due to sediment entrainment away from the bed and slower settling. Natural sediment in coastal zones has a variety of sediment sizes often classified as well-sorted (nearly uniform sizes) or poorly sorted (mixed sediment sizes). The response of well-sorted sediment particles can be characterized and predicted with a representative sediment diameter. However, the response of mixed sediment depends on the size fractions and the interaction of different size fractions with each other and with the flow field. Well-sorted and mixed sediment particles were simulated using a computational model with conditions representative of normal and storm waves. Mixed sediment with only 30% of the coarse fraction (70% of the medium fraction) responded similar to the well-sorted coarse sediment with slightly higher sediment fluxes due to the inverse vertical sorting (upward coarsening). Additionally, the medium particles serve as a smooth bed underneath coarse particles enhancing sediment entrainment.

1. Introduction

Predicting hydrodynamic evolution and the underlying morphodynamics shoreward of the wave shoaling zone is an ongoing challenge in coastal oceanography. Considerable effort has been made using regional-scale modeling tools to predict the hydrodynamics and the beach response to high energy storm events as well as beach recovery under low energy waves (Hegermiller et al., 2022; Rafati et al., 2021; Van der Lugt et al., 2019). These modeling frameworks, formulated as short-wave-averaged models, are not designed to simulate wave-by-wave hydrodynamic and sediment transport processes. Hence, key processes of intra-wave-driven sediment transport are not resolved, and the sediment transport modeling relies on empirical formulations parameterized by bulk wave characteristics (Kalra et al., 2019; Ruessink et al., 2012; Van der A et al., 2013; Van Rijn, 2007a, 2007b). Although there has been a great deal of progress in parameterizing wave-driven sediment transport, physical understanding on several important processes, such as the effect of particle size sorting, is lacking.

Gradients in cross-shore sediment transport fluxes lead to beach profile evolution. The main drivers of the cross-shore sediment fluxes are the skewed/asymmetric near-bed wave orbital velocities, the offshore-directed undertow currents, wave-breaking generated turbulence, and progressive wave streaming (Sherwood et al., 2021). Among these factors, the wave-induced sediment flux caused by skewed and asymmetric waves has been found to contribute significantly to the onshore sediment transport, shaping surf zone sand bars, and driving beach recovery (Brinkkemper et al., 2018; Pender & Karunarathna, 2013; Ruessink et al., 2016). Wave skewness/asymmetry and wave intensity increase from the wave shoaling region before peaking in the wave breaking zone and followed by a decreasing trend toward the inner surf zone (Elgar et al., 2001; Rafati et al., 2021; Ruessink et al., 2012).

Oscillatory flow tunnel experiments have been used to mimic the wave-induced near bed flow field and study the underlying bed sediment response. An advantage of flow tunnel experiments is the ability to study sediment transport with a desired sediment configuration under a wide variety of skewness/asymmetry and flow intensity representative of field observations (e.g., Liu & Sato, 2005; O'Donoghue & Wright, 2004a; Ruessink et al., 2011). Wave non-linearity drives the sediment onshore due to the larger flow velocity magnitude during the crest of the skewed waves (Ahmed & Sato, 2003a; O'Donoghue & Wright, 2004b; Ribberink & Al-Salem, 1994) and larger onshore flow acceleration of the asymmetric waves (Nielsen, 2006; Van der A et al., 2010; Watanabe & Sato, 2004).

For fine sand (median grain diameter d_{50} typically smaller than 0.2 mm) under oscillatory flow motion, phase-lags occur in sediment response to the boundary layer flows (Dohmen-Janssen et al., 2002; Dong et al., 2013). Accordingly, under skewed waves fine sediment particles are suspended above the sediment bed during the crest (onshore) interval while a large fraction does not settle back to the bed during the onshore-offshore flow reversal. As a result, a significant percentage of particles suspended during the crest interval are transported offshore during the trough (offshore) interval (O'Donoghue & Wright, 2004a, 2004b). Therefore, the net wave-period-averaged onshore sediment transport rate is lower for fine sand compared to that of medium (0.2 mm < d_{50} < 0.4 mm) and coarse sand (d_{50} > 0.4 mm) under the same oscillatory flow. Another mechanism influencing wave-driven onshore sediment transport is the generation of plug flow under high flow acceleration (or horizontal pressure gradient) (Berni et al., 2017; Sleath, 1999). Field and laboratory data indicate a relatively thick layer of sediment is entrained and transported as a nearly uniform block under high near-bed flow acceleration (Anderson et al., 2017; Flores & Sleath, 1998; Foster et al., 2006).

Sediment heterogeneity in the nearshore is an important factor in the sediment transport processes (Holland & Elmore, 2008; Schwartz & Birkemeier, 2004). Depending on the wave intensity, fine and coarse sediment particles respond differently to the flow field as they transport and settle in different locations in the cross-shore direction; causing well-sorted and mixed sediment size distributions locally (Huisman et al., 2016; Kaczmarek et al., 2004; Prodger et al., 2016; Stauble, 1992). In the past two decades, two-phase Eulerian-Lagrangian models have been used to simulate the sediment beds consisting of non-uniform sediment particle sizes under wave motions (Calantoni & Thaxton, 2008; Drake & Calantoni, 2001; Finn et al., 2016; Rafati et al., 2020). These studies showed that sediment beds consisting of uniform and non-uniform sediments respond differently to the wave-induced flows due to the sorting processes (Calantoni & Thaxton, 2008; Harada & Gotoh, 2008; Hassan & Ribberink, 2005; Rafati et al., 2020).

Although the main mechanisms of sediment entrainment and transport under nonlinear wave motions are well-studied, the findings, particularly regarding the phase lag effects and plug flow, have not been extended to mixed sediments driven by skewed and asymmetric flows. Using a two-phase Eulerian-Lagrangian model (Cheng et al., 2018; Rafati et al., 2020), we focus on the vertical sorting of mixed sediment beds consisting of medium and coarse sand subject to wave motion and the results are compared to those of well-sorted coarse sand and medium sand. The remaining sections of the manuscript are organized as follows. Information on the Eulerian-Lagrangian model formulation is given in Section 2. Model validation for well-sorted and mixed sand is presented in Section 3. In Section 4, the simulation results are introduced with a detailed analysis on the wave-averaged and intra-wave transport rates. In Section 5, a discussion is presented on quantifying the sheet flow layer thickness and some uncertainties in morphodynamic modeling due to sediment size characteristics. Concluding remarks are summarized in Section 6.

2. Model Description

The Eulerian-Lagrangian modeling framework solves the fluid phase (Eulerian) using SedFoam based on finite volume method (Cheng et al., 2017) developed using the OpenFOAM CFD toolbox, and the particle phase (Lagrangian) using LIGGGHTS based on the discrete element method (Kloss et al., 2012). The coupling between fluid and particle phase solvers is accomplished by CFDEM (Goniva et al., 2012). A brief overview of the governing equations and the closure models is given below (additional details in Cheng et al. (2018) and Rafati et al. (2020)).

In the particle phase, the position of each particle is tracked by solving the translational and rotational equations of motion, respectively,

$$m_i \frac{d\boldsymbol{v}_i}{dt} = \boldsymbol{f}_{d,i} + \left(\boldsymbol{f}_{x,i} - \nabla_i p\right) \cdot V_i + \sum_{j=1}^{N_c} \left(\boldsymbol{f}_{n,ij} + \boldsymbol{f}_{t,ij}\right) + m_i \boldsymbol{g}, \tag{1}$$

$$I_i \frac{d\boldsymbol{\Omega}_i}{dt} = \sum_{j=1}^{N_c} \left(\boldsymbol{\mathcal{M}}_{t,ij} + \boldsymbol{\mathcal{M}}_{r,ij}\right), \tag{2}$$

where $\boldsymbol{v}_i$ is the translational velocity of particle, $\boldsymbol{f}_{d,i}$ is the drag force acting on the particle i, $\boldsymbol{f}_{x,i}$ is the external body force driving the oscillatory flow applied to a particle, $\nabla_i p$ is the fluid pressure gradient interpolated at particle i, and V_i is the volume of particle i. The normal and tangential contact forces on particle i from particle j are expressed as $\boldsymbol{f}_{n,ij}$ and $\boldsymbol{f}_{t,ij}$, respectively, with N_c the number of particles in contact with particle i, and $m_i\boldsymbol{g}$ is the gravitational force. In 2, $\boldsymbol{\Omega}_i$ is the angular velocity of particle i, $\boldsymbol{M}_{t,ij}$ is the torque generated by the tangential force, and $\boldsymbol{M}_{r,ij}$ is known as rolling friction torque (Luding, 2008). Intergranular forces are calculated based on the soft sphere model (Cundall & Strack, 1979). The set of coefficients used in the DEM solver were specified previously (e.g., Rafati et al., 2020) including the Young's modulus as $E = 5 \times 10^6$ Pa, the restitution coefficient as $e = 0.5$, the Coulomb friction coefficient as $\mu_c = 0.5$, and the Poisson's ratio as $e = 0.45$.

In the fluid phase, the Reynolds-averaged momentum equation is written as

$$\frac{\partial \rho_f \left(1 - \overline{\phi}_s\right) \overline{\boldsymbol{u}}_f}{\partial t} + \nabla \cdot \left[\rho_f \left(1 - \overline{\phi}_s\right) \overline{\boldsymbol{u}}_f \overline{\boldsymbol{u}}_f\right] = \left(1 - \overline{\phi}_s\right) \boldsymbol{f}_x - \left(1 - \overline{\phi}_s\right) \nabla \overline{p} + \nabla \cdot \boldsymbol{\tau}_f + \rho_f \left(1 - \overline{\phi}_s\right) \boldsymbol{g} + \overline{\boldsymbol{F}}_d \tag{3}$$

where the overbar denotes the ensemble-average operator, ρ_f is the fluid density , $\overline{\boldsymbol{u}}_f$ is the fluid velocity, $\overline{\phi}_s$ is the sediment concentration, $\overline{\boldsymbol{F}}_d$ is the drag force of particles averaged in a fluid cell, and $\boldsymbol{\tau}_f$ is the total fluid stress tensor. The average drag force is calculated by averaging the drag forces on the particles within a fluid cell. To account for the turbulence-induced particle suspension, the eddy interaction model (Graham & James, 1996) was used which previously showed good skill in modeling the turbulent suspension in steady (Cheng et al., 2018) and oscillatory (Rafati et al., 2020) sheet flow simulations. The fluid shear stress is calculated as the sum of the viscous stress and turbulent Reynolds stress, where the Reynolds stress is calculated based on eddy viscosity using k-ε model. The transport equations for the turbulent kinetic energy k and turbulent dissipation rate ε have been presented previously (Cheng et al., 2017; Rafati et al., 2020). Here, a previously used set of empirical coefficients for the closure models was implemented (Rafati et al., 2020).

3. Model Validation

Model validation was performed using laboratory data (Hassan & Ribberink, 2005) on well-sorted and mixed sands under velocity-skewed oscillatory flows. Model simulations were performed for the sediment beds consisting of the spherical particles with the size distributions identical to those used in the laboratory (Hassan & Ribberink, 2005) for the well-sorted medium sands with $d_{50} = 0.21$ mm (Table 1: cases B7, B8, and B9) and $d_{50} = 0.34$ mm (Table 1: cases R1, R2, and R3) as well as for the mixed sand with a bimodal size distribution consisting of 70% medium fraction and 30% coarse fraction (Table 1: cases P1, P2, and P3). It is worth noting that the errors reported in measurements of net transport rates for well-sorted and mixed sands in the laboratory (Hassan & Ribberink, 2005) range from about 10% to about 30%. Compared to the model validation presented

Table 1
Test Cases by Hassan and Ribberink (2005) Used for Validation

Case ID	Sediment characteristics	U_{rms} (m/s)
B7	Well-sorted (σ_g = 1.29 sand) of d_{50} = 0.21 mm	0.50
B8		0.70
B9		0.92
R1	Well-sorted (σ_g = 1.28 sand) of d_{50} = 0.34 mm	0.59
R2		0.68
R3		0.89
P1	Mixed sand (σ_g = 2.67), 70% medium sand (d_{50} = 0.21 mm) and 30% coarse sand (d_{50} = 0.97 mm)	0.59
P2		0.64
P3		0.85

in Rafati et al. (2020), here the model validation was further expanded to simulate a wider variety of grain sizes ranging from 0.21 to 0.97 mm under different flow conditions.

We assumed sheet flow to be fully developed in the streamwise (x) and spanwise (y) directions. Accordingly, one grid cell is used in streamwise and spanwise direction in the fluid model domain (1DV simulation) and the periodic lateral (x and y directions) boundary conditions are applied for fluid velocity and sediment particles. The bottom and the top boundaries were assigned as no-slip wall and the shear-free symmetric boundary, respectively. An immobile sediment layer at the bottom of the model domain is established by placing very dense particles (density of 26,500 kg/m^3) with a diameter twice the median grain diameter of the mixture (Rafati et al., 2020). The domain size was chosen following Rafati et al. (2020) to be $l_x = 20d_{50}$ and $l_y = 10d_{50}$, where l_x and l_y represent the domain length in streamwise and spanwise directions, respectively. The sketches of particles in the simulation domain for the initial bed are shown for the well-sorted distributions (Figures 1b and 1c) and the bimodal distribution (Figure 2b). For all the cases investigated here, different sizes of particles are well-mixed in the initial sediment bed. Free stream velocity in the fluid model is implemented with the body force $\boldsymbol{f}_x$ from 3, as $\boldsymbol{f}_x = -\rho \frac{dU}{dt}$, where U is the free stream velocity. The body force is also applied to the sediment particles as $\boldsymbol{f}_{x,i} = -\rho \frac{dU}{dt}$ from 1.

3.1. Well-Sorted Sand

The model was validated for the well-sorted medium sands using the B series (Table 1, d_{50} = 0.21 mm) and R series (Table 1, d_{50} = 0.34 mm) from the laboratory (Hassan & Ribberink, 2005) under different flow conditions with the root-mean-square free stream velocity U_{rms} ranging from 0.50 to 0.92 m/s (B series) and from 0.59 to 0.89 m/s (R series), all having the same velocity skewness $\beta = U_{max}/(U_{max} - U_{min}) = 0.65$ and oscillatory flow period of 6.5 s. The domain size was assigned as l_x = 4 mm, l_y = 2 mm, and l_z = 400 mm (B series, d_{50} = 0.21 mm, Figure 1b), and l_x = 7 mm, l_y = 4 mm, and l_z = 400 mm (R series, d_{50} = 0.34 mm, Figure 1c). The grid size in the vertical direction (dz) was assigned to be close to d_{50}. Accordingly, dz = 0.25 mm and dz = 0.3 mm were used in the bottom 50 mm of the domain for series B and series R, respectively. Above the bottom layer, the grid size increased linearly to dz = 1 mm (Series B) and dz = 1.5 mm (Series R) toward the top of the domain (z = 0.4 m). Figure 1a shows a good agreement between modeled and measured wave-period-averaged (or wave-averaged) net sediment transport rates for the cases with d_{50}= 0.21 mm (B series, blue circles) and d_{50} = 0.34 mm (R series, red squares). The model is capable of predicting the net sediment transport rates for the well-sorted medium sands driven by velocity skewed waves where the differences between the model predictions and measured data are within 25%.

3.2. Mixed Sand

The model was further validated for a mixed sand condition with a bimodal distribution corresponding to P series (Table 1) from the laboratory (Hassan & Ribberink, 2005) with 30% of coarse fraction with d_{50} = 0.97 mm and

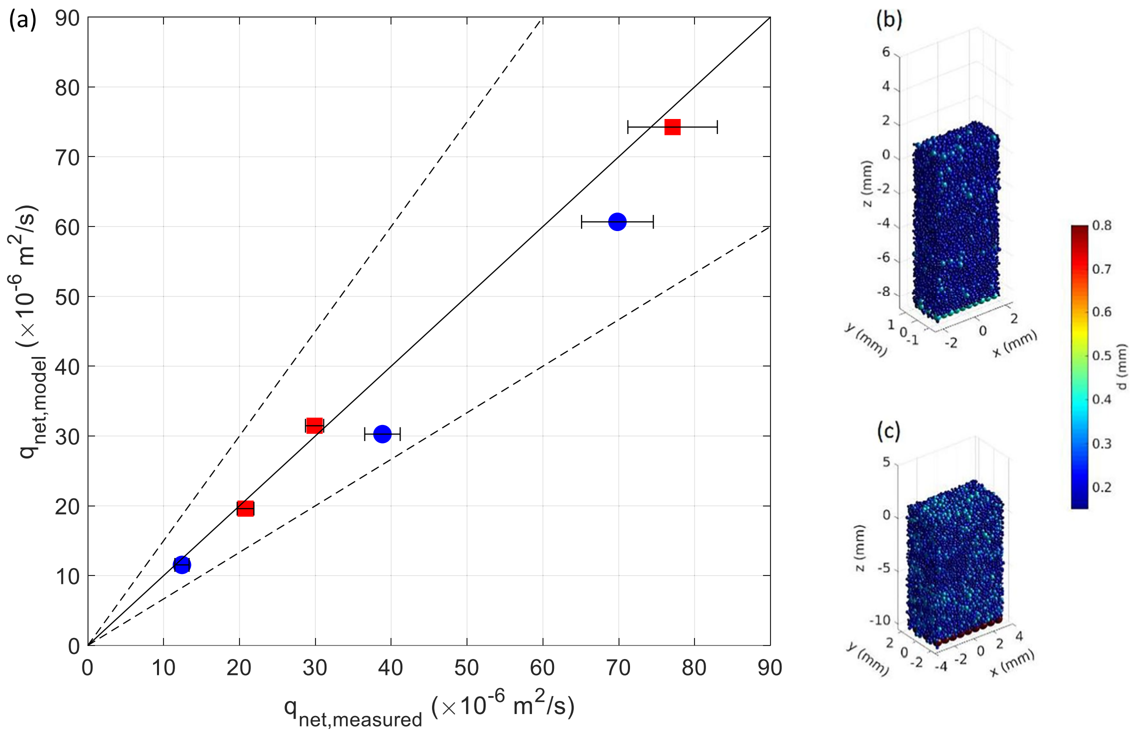

Figure 1. (a) Wave-averaged sediment transport rates of well-sorted sands with median grain sizes of d_{50} = 0.21 mm (B series, blue circles) and d_{50} = 0.34 mm (R series, red squares) simulated using oscillatory flows from the laboratory (Hassan & Ribberink, 2005). Solid line shows the one-to-one correspondence, and the dashed lines have slopes of 3/2 and 2/3 signifying the 50% agreement. (b–c) Shown are snapshots of initial sediment bed in the simulation domain corresponding to B series and R series, respectively. The horizontal lines denote the error bars reported in laboratory data.

70% of medium fraction with d_{50} = 0.21 mm. The laboratory tests on the mixed sand were performed under oscillatory flow motions with U_{rms} = 0.59–0.85 m/s, all having the same velocity skewness β = 0.65. The model domain size was l_x = 6 mm, l_y = 3 mm, and l_z = 400 mm (Figures 2b and 2c). For the mixed sand cases the grid size in the vertical direction was set to dz = 0.3 mm in the bottom 50 mm of the simulation domain which was closer to the median grain diameter of medium fraction (d_{50} = 0.21 mm). The grid size was linearly increased to dz = 1.5 mm toward the top of the simulation domain at z = 40 mm. Figure 2c shows the configuration of the particles after five wave periods where the vertical sorting as an inverse grading was evident with coarse particles covering the bed surface and the fine particles hidden below (compare with Figure 2b for a well-mixed initial particle bed). Figure 2a shows wave-averaged net fractional transport rates between the model results and the laboratory data. The model was capable of predicting the net fractional transport rates for the mixed sand under all the wave intensities (U_{rms} = 0.59–0.85 m/s) from the laboratory tests (Hassan & Ribberink, 2005) where the differences between the model predictions and measured data are within 50%. Compared to the errors in measurements (10%–30%) model results show good skill in predicting the fractional transport rates.

4. Results

4.1. Design of Simulations

Twenty-four sets of numerical simulations were performed to investigate the response of sediment beds consisting of different sediment size characteristics to a variety of oscillatory flows. Three sediment size characteristics (Table 2) were simulated including the well-sorted medium (WS-M, d_{50} = 0.21 mm), well-sorted coarse (WS-C, d_{50} = 0.97 mm), and mixed sand with a bimodal distribution (BM, consisting of 70% WS-M and 30% WS-C). Eight flow conditions were studied (Table 3) with U_{rms} values of 0.64 and 0.85 m/s and β values of 0.57, 0.65, 0.71, and 0.78. These wave conditions cover a wide range of the third moment velocities $<U^3>$ from 0.08 to 0.88 m^3/s^3. The studied oscillatory flow conditions were similar to the near-bed flow intensity and skewness measured in the large wave flume experiments under breaking and non-breaking waves (e.g., Mieras et al., 2017;

Version of record at: https://doi.org/10.1029/2022JC018686

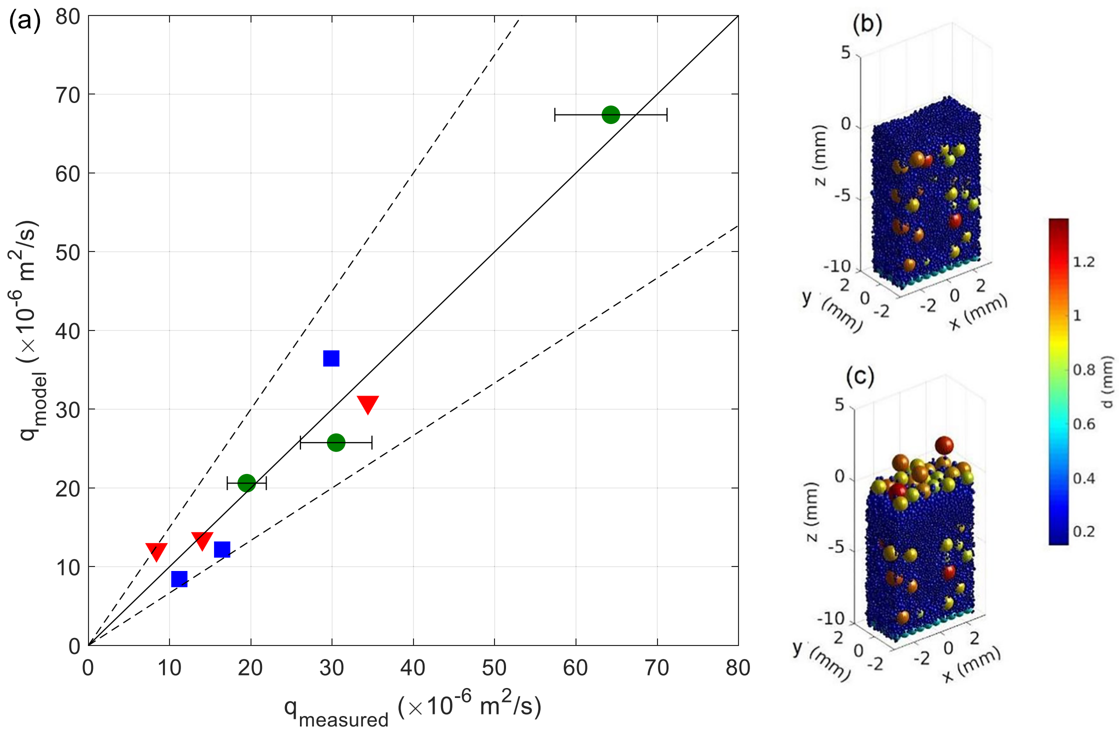

Figure 2. (a) Wave-averaged fractional (blue squares and red triangles) and total (green circles) sediment transport rates of mixed sand with bimodal size distribution (P series) composed of 70% medium fraction with $d_{50} = 0.21$ mm (blue squares) and 30% coarse fraction with $d_{50} = 0.97$ mm (red triangles) simulated using oscillatory flows from the laboratory (Hassan & Ribberink, 2005). Solid line shows the one-to-one correspondence, and the dashed lines have slopes of 2/3 and 3/2 signifying the 50% agreement. (b–c) Shown are snapshots of the initial sediment bed and the sediment bed after five waves, respectively, corresponding the the mixed sand. The horizontal lines denote the error bars reported in laboratory data.

Schretlen, 2012; Van der Zanden et al., 2016) as well as field measurements in the shoaling zone toward inner surf zone under high-energy and low-energy waves (e.g., Gallagher et al., 1998; Rafati et al., 2021). The wave skewness, S_k, is calculated using the third moments of the free stream velocity as (Elgar et al., 1988),

$$S_k = \frac{\langle U^3 \rangle}{\langle U^2 \rangle^{3/2}}, \tag{4}$$

where U is the prescribed free stream velocity and the angle brackets denote the time averaging over a wave period. An analytical formula (Abreu et al., 2010) was used to generate the free stream velocity time series with the desired U_{rms} and S_k values

$$U(t) = U_w f \frac{\left[sin(\omega t) + \frac{r sin\phi}{1+\sqrt{1-r^2}} \right]}{[1 - rcos(\omega t + \phi)]}, \tag{5}$$

where U_w is the amplitude of the wave orbital velocity, r is an index of nonlinearity ($r = 0$ corresponds to linear wave orbital velocity), f is a function of r ($f = \sqrt{1 - r^2}$), ω is the frequency, and ϕ is the waveform parameter set to $-90°$ for velocity-skewed waves.

The maximum Shields parameter at the peak wave crest was calculated (Soulsby, 1997) to quantify the mobility of the sediment particles (see Appendix in Rafati et al. (2020)) for different sediment size characteristics (Table 4). A phase-lag parameter (Dohmen-Janssen et al., 2002) was calculated for quantification of phase lags between sediment concentration and the boundary layer flow field. Since the calculation of both Shields parameter and

Table 2
Simulated Particle Size Characteristics

Distribution	Category	d_{10} (mm)	d_{50} (mm)	d_{90} (mm)	σ_g
WS-M	well-sorted medium	0.15	0.21	0.29	1.29
WS-C	well-sorted coarse	0.85	0.97	1.20	1.32
BM[a]	bimodal	0.16	0.24	0.99	2.67

[a]The BM distribution consists of 70% WS-M and 30% WS-C.

Version of record at: https://doi.org/10.1029/2022JC018686

Table 3
Simulated Oscillatory Flow Conditions

Wave ID	T (s)	T_{crest} (s)	U_{rms} (m/s)	β	S_k	$<U^3>$ (m^3/s^3)	U_{crest} (m/s)	U_{trough} (m/s)
I64B57	6.5	2.95	0.64	0.57	0.30	0.08	1.04	−0.79
I64B65	6.5	2.67	0.64	0.65	0.59	0.15	1.14	−0.61
I64B71	6.5	2.35	0.64	0.71	0.98	0.26	1.42	−0.58
I64B78	6.5	2.01	0.64	0.78	1.43	0.38	1.70	−0.48
I85B57	6.5	2.95	0.85	0.57	0.30	0.18	1.38	−1.04
I85B65	6.5	2.67	0.85	0.65	0.59	0.36	1.51	−0.81
I85B71	6.5	2.35	0.85	0.71	0.98	0.60	1.88	−0.77
I85B78	6.5	2.01	0.85	0.78	1.43	0.88	2.26	−0.64

phase-lag parameter were based on a sinusoidal wave shape, the entire flow cycle was assumed to be a sine wave having the orbital velocity amplitude the same as that of peak flow crest (U_{crest}) with a wave period of $T_{wave} = 2T_{\mathrm{crest}}$ (T_{crest} being the crest interval, Table 3). For the simulations with BM distributions, the median grain diameter of the coarse fraction ($d_{50} = 0.97$ mm) was used in the calculations of the Shields parameter and phase lag parameter due to the bed surface layer being dominated by the coarse fraction (Figure 2c).

4.2. Net Sediment Transport Rates

Wave-averaged net sediment transport rates for all 24 cases were plotted as a function of the third moment of velocity $<U^3>$ for the well-sorted medium (WS-M), well-sorted coarse (WS-C), and bimodal distribution (BM) (Figure 3, values reported in Table 5). The wave-averaged net sediment transport rate is highly correlated with $<U^3>$ as was found in oscillatory water tunnel studies (Hassan & Ribberink, 2005; Ribberink & Al-Salem, 1994) and in large wave flume experiments under non-breaking (Schretlen, 2012), breaking (Van der Zanden et al., 2017), and near-breaking (Mieras et al., 2019) waves. For the well-sorted coarse sand (WS-C, $d_{50} = 0.97$ mm, red triangles in Figure 3), the net transport rates follow a linear trend with $<U^3>$. The net transport rates for the low-energy wave motions ($<U^3> \leq 0.26$ m^3/s^3) for different sediment size distributions are also similar and follow the same linear trend as a function of $<U^3>$. However, for higher energy conditions ($<U^3> \geq 0.36$ m^3/s^3), the well-sorted medium sand (WS-M) cases deviate from the linear trend toward lower net transport rates. For the highest wave energy case (I85B78, $<U^3> = 0.88$ m^3/s^3), the net transport rate of WS-M becomes 44% lower than that of the well-sorted coarse sand case. The reduction of the net (onshore) transport rate for WS-M as velocity skewness increased may be attributed to the phase-lag effects that can be quantified by the phase lag parameter (Dohmen-Janssen et al., 2002) (see Table 4). For higher values of the phase lag parameter ($\theta_{max} d_{50}\omega/w_s \gtrsim 0.042$), the net transport rates of WS-M fall notably behind those of WS-C. The results were consistent with the threshold value of $\theta_{max} d_{50}\omega/w_s = 0.038$ (Dohmen-Janssen et al., 2002). Lower net transport rate of WS-M under waves with high velocity skewness is also consistent with the previous measurement of coarse ($d_{50} = 0.465$ mm) and fine ($d_{50} = 0.125$ mm) sand under velocity skewed flows (analyzed by Shimamoto (2016)). Interestingly, for the BM consisting of only 30% coarse fraction, the trend of the net transport rate as a function of $<U^3>$ is similar to that of WS-C. The results of BM were consistent with laboratory observations of mixed sands under velocity-skewed waves with a smaller wave period of 3 s and velocity skewness of $\beta = 0.7$ (Dibajnia & Watanabe, 1996). Model results presented here further show that for a wider range of wave velocity skewness and intensity, the transport rates of the mixed sediment were consistently similar to those of coarse fraction. However, looking toward a more quantitative understanding, we observed that the net transport rates of the BM were always higher than those of the WS-C (about 18% higher on average over the simulated wave conditions) which was found to be due to the generation of plug flow. In the following subsections, we provide more analysis and explanation on the sediment transport rates presented in Figure 3.

Table 4
Maximum Shields Parameter and Phase Lag Parameter of Dohmen-Janssen et al. (2002) for the Simulated Cases

	θ_{max}			$\theta_{max} d_{50}\omega/w_s$		
Wave ID	WS-M	WS-C	BM	WS-M	WS-C	BM
I64B57	1.41	0.47	0.47	0.011	0.004	0.004
I64B65	1.67	0.55	0.55	0.015	0.005	0.005
I64B71	2.53	0.83	0.83	0.025	0.009	0.009
I64B78	3.63	1.19	1.19	0.042	0.015	0.015
I85B57	2.30	0.74	0.74	0.018	0.006	0.006
I85B65	2.75	0.89	0.89	0.024	0.009	0.009
I85B71	4.18	1.34	1.34	0.042	0.015	0.015
I85B78	6.01	1.92	1.92	0.070	0.025	0.025

4.3. Intra-Wave Sediment Transport

Time series of sediment transport rates for WS-M, WS-C, and BM distributions (Table 2) are shown in Figure 4 for the wave conditions of low wave intensity and low wave skewness (Figure 4d, I64B57, $U_{rms} = 0.64$ m/s, $S_k = 0.30$), high wave intensity and low wave skewness (Figure 4e, I85B57, $U_{rms} = 0.85$ m/s, $S_k = 0.30$), and high wave intensity and high wave skewness (Figure 4f, I85B78, $U_{rms} = 0.85$ m/s, $S_k = 1.43$).

During the acceleration phase from the flow reversal at $t = 0$ to shortly before the peak flow, the sediment fluxes were similar for different sediment size distributions in all three flow conditions (Figures 4d–4f). The main differences were observed near the peak flow crest and deceleration phase. For the case with the low wave intensity and low wave skewness (Figure 4d), sediment flux of WS-C was significantly lower than that of WS-M at the peak

Version of record at: https://doi.org/10.1029/2022JC018686

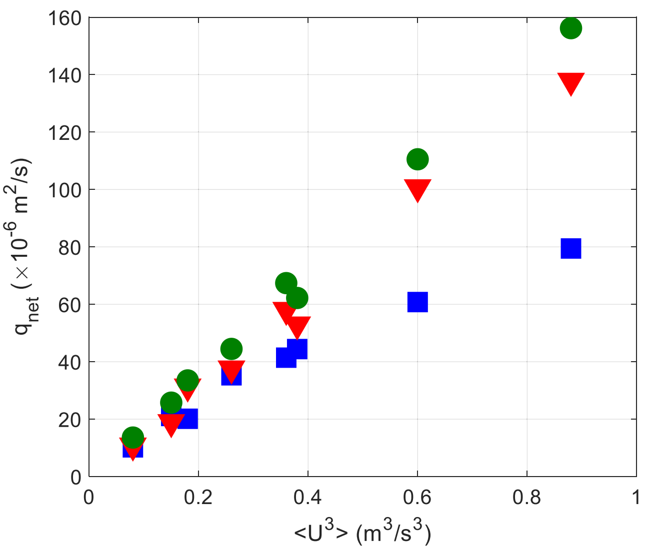

Figure 3. Wave-averaged net sediment transport rates versus the third moment of free stream velocity $<U^3>$ for each wave condition shown in Table 3 for the simulated sediment size distributions (Table 2) of well-sorted medium sand (WS-M, $d_{50} = 0.21$ mm, blue squares), well-sorted coarse sand (WS-C, $d_{50} = 0.97$ mm, red triangles), and mixed sand with bimodal size distribution (BM, 70% of medium sand and 30% of coarse sand, green circles).

flow crest, which may be explained by the corresponding values of maximum Shields parameter (Table 4) being about 3 times smaller for the WS-C distribution. Interestingly, under the same flow condition, the sediment flux of the BM distribution was notably larger than that of WS-C and more similar to WS-M (Figure 4d). For the cases with high wave intensity and low wave skewness (Figure 4e), the sediment fluxes of WS-M and WS-C become similar, while the sediment flux of BM remains the largest. For the cases of high wave intensity and high wave skewness (Figure 4f), the sediment flux of WS-M at the peak flow crest ($t = 1$ s) is about 30% lower than those of WS-C and BM, although the maximum Shields parameter of WS-M is 3 times larger than that of WS-C. For the BM distribution with 70% of medium sand fraction, sediment fluxes during the crest interval were persistently large, if not the largest, for all three wave conditions. We observed the formation of a high mobility, predominantly coarse sand transport layer for the BM distribution under high energy wave conditions (See Section 4.4) above a relatively soft foundation formed by the medium sand particles (Ahmed & Sato, 2003b, see also Figure 2c). Finally, during the flow deceleration (shortly after the peak flow and before the crest-trough reversal), the sediment flux of WS-C was lower than those of WS-M and BM distributions for all three flow conditions.

The sediment fluxes during the trough (offshore flow) periods were qualitatively similar for all flow conditions with the WS-M distribution having the largest transport flux, followed by the BM and the WS-C distributions. The transport fluxes during the trough period were consistent with the higher mobility of medium sand particles in WS-M compared to the lower mobility of the coarse sand particles in WS-C and on the surface layer of the bed in the BM distribution (see Figure 2c) known as the armoring effect (Rafati et al., 2020; Wiberg et al., 1994). Under high velocity-skewness (Figure 4f) during the trough period, sediment fluxes of BM and WS-C were both small. The results were consistent with the relatively low flow intensity during the wave trough ($U_{trough} = -0.64$ m/s), which can barely mobilize the coarse particles on the bed surface of the BM and WS-C distributions.

In the following, more comprehensive discussion on these simulations will be given by answering the following questions,

1. Why does the transport rate of the WS-M distribution during the crest interval fall behind those of BM (having 70% medium fraction) and WS-C for the high wave intensity and skewness condition? This question addresses the effect of phase lags in sediment entrainment and settling intervals.
2. Why is the transport rate of the WS-C distribution smaller during the deceleration interval for all three wave conditions? Through investigating this question in the WS-C distribution, we understand the effect of bedload dominance in the transport of coarse sand.
3. Why is the transport rate of the BM distribution the largest during the crest interval for all three wave conditions? By addressing this question, we gain insight into the effect of plug flow generated in the BM distribution.

Table 5
Wave-Averaged Net Sediment Transport Rates for the Simulated Flow Conditions and Sediment Size Distributions Reported in mm²/s

Wave ID	WS-M	WS-C	BM
I64B57	10.2	10.8	13.6
I64B65	21.1	18.9	25.8
I64B71	35.3	37.6	44.5
I64B78	46.3	53.0	62.2
I85B57	19.5	31.35	33.5
I85B65	41.3	58.0	67.4
I85B71	61.5	100.8	110.5
I85B78	77.6	137.85	153.0

Additional model results from intra-wave simulations of sediment entrainment and deposition illustrated how sediment beds of well-sorted and mixed size distributions respond to wave forcing. The focus hereafter is on the crest interval since the trend of sediment fluxes during trough interval more or less follow the general expectation.

Figures 5 and 6 present the sediment horizontal fluxes and particle distributions under the high wave intensity and high velocity skewness condition (I85B78) for WS-M, WS-C, and BM distributions at the instants of flow

Version of record at: https://doi.org/10.1029/2022JC018686

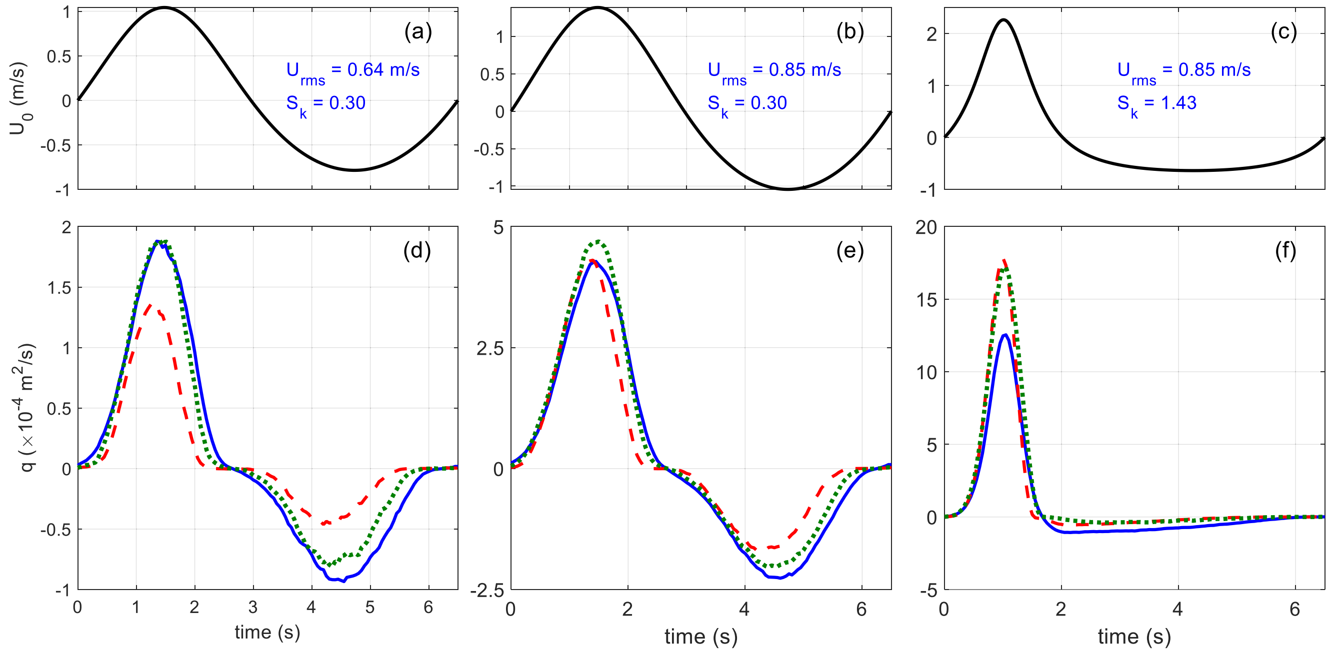

Figure 4. Free stream velocity time series for (a) low wave intensity and low velocity skewness (I64B57), (b) high wave intensity and low velocity skewness (I85B57), and (c) high wave intensity and high velocity skewness (I85B78). (d–f) Corresponding time series of intra-wave sediment transport rates for the well-sorted medium sand (d_{50} = 0.21 mm, solid blue), well-sorted coarse sand (d_{50} = 0.97 mm, dashed red), and mixed sand with bimodal size distribution (70% of medium and 30% of coarse, dotted green).

acceleration (circle in Figure 5a), peak crest (square), deceleration (diamond), and crest-trough reversal (triangle). The percentages of depth-integrated fluxes in the bedload (or near-bed load) regime (below the dotted black lines in Figures 5b–5d) at different instants for each size distribution also were calculated. The volumetric sediment concentration of 0.08 m^3/m^3 is used to distinguish between the bedload and suspended load regimes (Figures 5b–5d, horizontal dotted lines), consistent with previous studies (O'Donoghue & Wright, 2004a). During flow acceleration, all size distributions showed similar response to the flow field with sediment particles located mainly near the bed (Figures 6a, 6e, and 6i) and the large onshore-directed (positive) sediment fluxes dominated by bedload transport (Figure 5b, bedload fraction above 83%), which is consistent with the time series of sediment transport rates during the acceleration period (Figure 4f, 0 s < t < 1 s).

For the WS-M distribution the bedload fraction decreased from 83% at the flow acceleration (Figure 5b, solid blue) to 76% at the peak crest (Figure 5c) and to 31% during the flow deceleration (Figure 5d). The transition can be clearly observed in the sketches of the particles for WS-M (Figures 6a–6c). The different sediment transport regimes during the acceleration and deceleration phases with the same free stream velocity has been referred to as "concentration asymmetry" (Dohmen-Janssen et al., 2002; Liu & Sato, 2005). The concertation asymmetry might be attributed to the "delayed entrainment" of the sediment particles during the relatively short period of the crest. It can be inferred that under high velocity skewness, sediment entrainment of the WS-M lags the near-bed flow field, which signifies the lower depth-integrated sediment fluxes of WS-M compared to those of WS-C and BM near the peak crest (see Figure 4f, 0.7 s < t < 1.3 s). The delayed entrainment observed in the present simulation was consistent with previous flow tunnel experiments on medium and fine sands (Dohmen-Janssen, 1999; Dong et al., 2013). It has been argued that when the sediment entrainment time (crest interval here) is relatively short, the sediment particles do not have enough time to become entrained as they could, given enough time under the oscillatory flow with the same crest velocity and longer crest interval. The sediment particles in the WS-M simulation with high wave intensity and high velocity skewness (Figures 4f, 5, and 6) experienced a similar condition of insufficient time for entrainment due to a relatively short crest interval. However, during flow reversal, there were a large number of particles in suspension for the WS-M distribution (Figure 6d). Accordingly, during the flow reversal, there was a significant amount of WS-M sediment flux in both suspension and the near-bed region (Figure 5e), which was higher than those of WS-C and BM distributions resulting from the phase-lag effect in sediment settling for medium sand.

Version of record at: https://doi.org/10.1029/2022JC018686

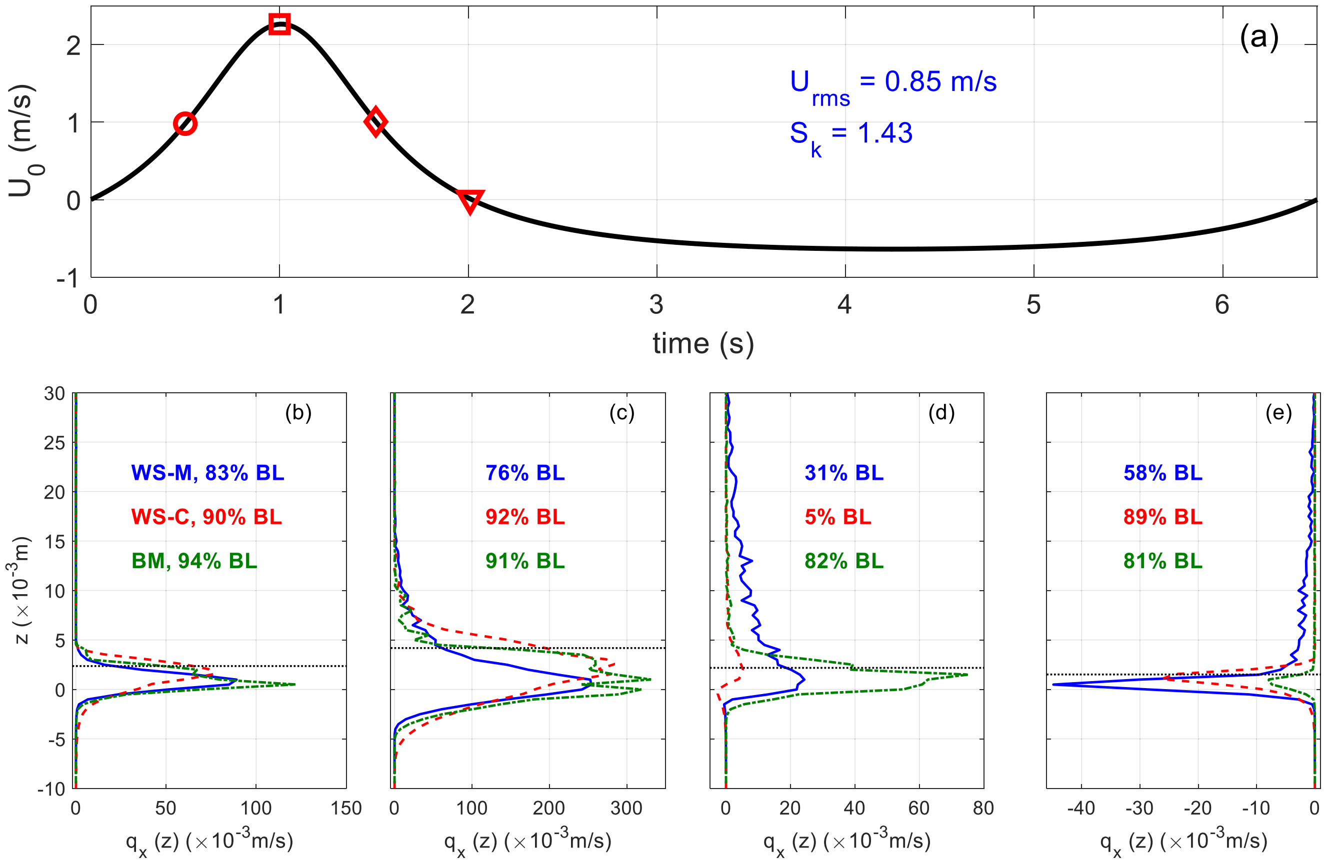

Figure 5. (a) Free stream velocity of the flow I85B78 with high wave intensity and high velocity skewness. Sediment flux profiles of WS-M (solid blue), WS-C (dashed red), and BM (dash-dot green) distributions are shown at the instants of acceleration (b, circle in a), peak flow crest (c, square in a), deceleration (d, diamond in a), and crest-trough reversal (e, triangle in a). The horizontal dotted lines denote the volumetric sediment concentration of 0.08 m^3/m^3.

For the WS-C distribution, bedload was the dominant regime of sediment transport during the onshore acceleration (Figure 5b, red dashed) and the peak flow crest (Figure 5c). Interestingly, for WS-C the sediment flux during the flow deceleration (Figure 5d) was smaller than the flux during the flow acceleration (Figure 5b), which can be explained by the faster settling (higher settling velocity) of coarse sediment particles and the dominance of bedload transport. From a snapshot of WS-C at flow reversal (Figure 6h) one can deduce that the sediment particles are no longer suspended. However, the sediment flux profile at flow reversal (Figure 5e) showed minor sediment flux of WS-C in the near-bed region ($z < 2$ mm), which can be attributed to the near-bed flow velocity leading the free stream velocity.

For the BM distribution, consisting of 70% medium fraction (d_{50} = 0.21 mm) and 30% coarse fraction (d_{50} = 0.97 mm), both size fractions played a role in entrainment and transport of the sediment particles. Consistent with previous measurements of mixed sediment under wave motion (Hassan & Ribberink, 2005; Nielsen, 1983), it is seen that for BM distribution the particles in suspension are mainly of medium fraction while coarse fraction is dominant near the bed (Figures 6j, 6k, and 6l). Similar to the WS-M distribution, sediment particles from the BM distribution show concentration asymmetry with sediment flux being mainly in the bedload region during the flow acceleration (Figures 5b and 6i) and a relatively thick layer (4~5 mm) of sediment flux (of bedload and small suspended load) during the peak flow crest (Figures 5c and 6j). However, a much larger near-bed sediment flux associated with the BM distribution was observed during the flow deceleration (Figures 5d and 6k). As the coarse fraction dominates the surface layer of BM distribution, the medium fraction underneath acts as a soft, smooth layer under the active layer that facilitates the transport of the sediment particles in the active layer (Ahmed & Sato, 2003b; also discussed in reference to Figure 7). It is worth noting that for the BM distribution the suspended load fraction was smaller compared to the WS-M distribution at the peak flow crest (Figure 5c) and deceleration (Figure 5d) due to the inverse grading with medium sand particles being armored by the coarse sand

Version of record at: https://doi.org/10.1029/2022JC018686

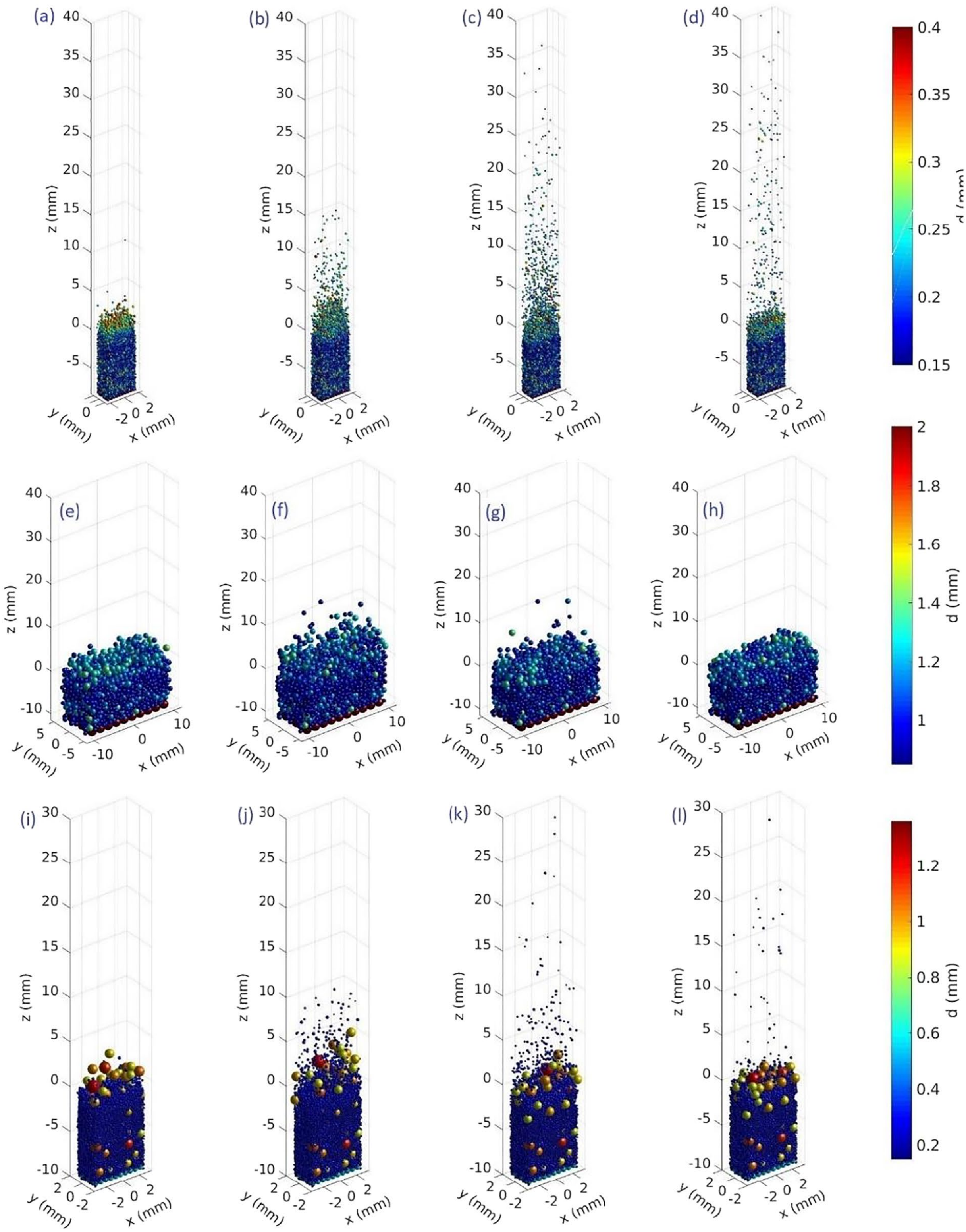

Figure 6. Snapshots of particles in the simulation domain shown under high wave intensity and high velocity skewness flow (I85B78) for WS-M (a-d, color scale ranges from 0.15 to 0.4 mm), WS-C (e-h, color scale ranges from 0.85 to 2 mm), and BM (i-l, color scale ranges from 0.15 to 1.3 mm) at instants of acceleration (a, e, i, circle in Figure 5a), peak flow crest (b,f,j, square in Figure 5a)), deceleration (c, g, k, diamond in Figure 5a)), and crest-trough flow reversal (d, h, l, triangle in Figure 5a).

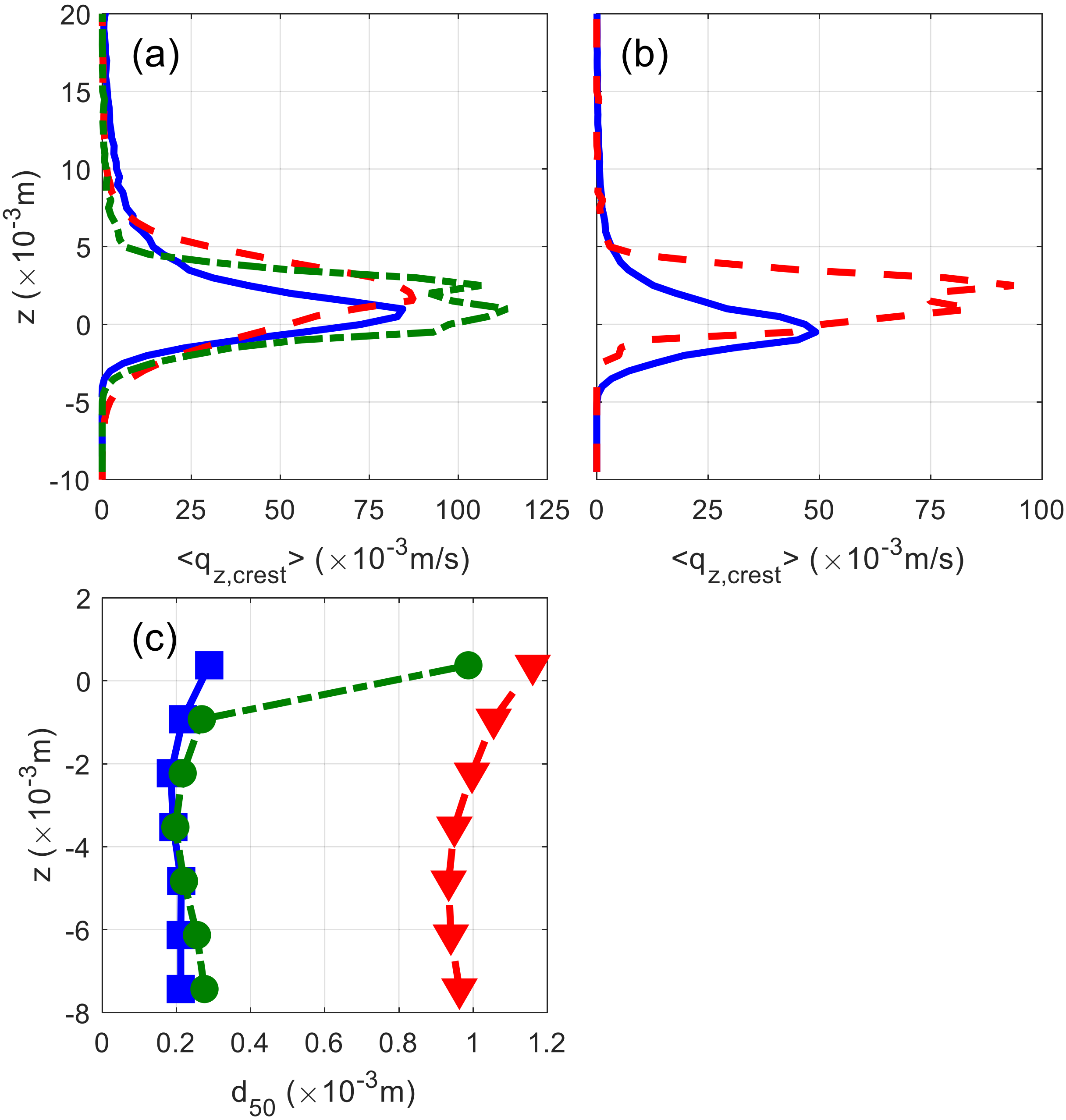

Figure 7. (a) Crest-averaged sediment flux profiles of WS-M (solid blue), WS-C (dashed red), and BM (dash-dot green) distributions shown under flow I85B78. (b) Crest-averaged sediment flux profiles corresponding to the medium fraction (solid blue) and coarse fraction (dashed red) of BM distribution under flow I85B78. (c) Vertical distribution of median grain diameter is shown in the sediment beds of WS-M (blue squares), WS-C (red triangles), and BM (green circles) distributions.

(Rafati et al., 2020) (see Figures 6b, 6c, 6j, and 6k). The armoring effect may be responsible for the negligible phase lag effects observed in the BM distribution during the flow reversal (Figures 5e and 6l). It can be concluded that dominance of the coarse fraction, armoring effect on the fine fraction, and the smooth layer provided by the medium fraction causes higher flux of the BM distribution in the near-bed layer and explains the BM distribution having the highest net sediment transport rates under the most energetic waves. The different bed responses of WS-M compared to BM and WS-C also may be attributed to the different sediment transport regimes. For WS-C and BM distributions where the transport is dominated by the coarse particles near the bed, sediment mobilization and transport is correlated with the intense particle collisions near the bed (Calantoni & Puleo, 2006; Schmeeckle et al., 2001). However, for the WS-M distribution, particle suspension induced by intense fluid turbulence was effective in sediment pick up and transport (Balachandar & Eaton, 2010), and thus sediment suspension played a more effective role in entrainment and transport processes.

4.4. Plug Flow Formation

To further investigate the larger sediment flux of the BM distribution compared to those of WS-M and WS-C distributions, the sediment flux profile of the BM distribution averaged over the crest interval ($<q_{z,crest}>$) was compared to those of WS-M and WS-C driven by the wave with the highest intensity and skewness (I85B78) (Figure 7a). Below $z = -1$ mm, the crest-averaged sediment fluxes of BM and WS-M distributions (blue and green curves in Figure 7a) had similar trends and values while the flux of WS-C distribution was distinct from the others. The similar sediment fluxes of WS-M and BM distributions can be explained by their similar vertical profile of median grain diameter below $z = -1$ mm (Figure 7c). Above $z = -1$ mm and up to $z = 4$ mm, the $<q_{z,crest}>$ of the BM distribution was notably higher than those of WS-M and WS-C. For the WS-C distribution, $<q_{z,crest}>$ peaked near $z = 2$ mm (Figure 7a, dashed-red curve), where for the WS-M distribution, $<q_{z,crest}>$ was of smaller magnitude and it peaked at about $z = 1$ mm (Figure 7a, solid-blue curve) and decreased rapidly away from it, consistent with the delayed entrainment discussed previously. Interestingly, the crest-averaged sediment flux of the BM distribution exceeded 0.09 m/s between $z = -1$ to 3 mm, which is a relatively thick high mobility layer of about 4 mm near the bed. Simulation results suggested the generation of plug flow (e.g., Sleath, 1999) for the BM distribution where a thick block of sediment was transported under intense flow acceleration. However, the plug flow formation obtained here may have been facilitated by vertical size gradation. First, by examining the vertical distribution of median grain diameter d_{50} within the sediment bed (Figure 7c), an inverse size gradation (upward coarsening) associated with the BM distribution was observed. The surface layer ($z \sim 0$ mm) was dominated by the coarse fraction (d_{50} close to 0.97 mm) and just below the surface layer (-5 mm $< z < 0$ mm) the grain sizes were close to that of medium fraction (d_{50} close to 0.21 mm). The fractional fluxes of the BM distribution (Figure 7b) revealed an intense flux of the coarse fraction above $z \sim 0$ mm (red-dashed curve, peaks at about 0.085–0.095 m/s), which was on top of a weaker flux of the medium fraction (solid blue curve). Model results revealed that in the BM distribution, plug flow of predominately coarse fraction occurred above a relatively smooth layer consisting mainly of the medium fraction. Since this plug flow feature was not seen in the WS-C distribution, it can be concluded that the inverse vertical grading of the BM distribution encourages plug flow formation.

The formation of plug flow has been attributed to intense pressure gradients (causing flow acceleration) quantified by the Sleath parameter as $S = -\frac{dp}{dx} / (\rho_s - \rho)\, g$. The critical Sleath parameter takes on a range of values from 0.3 to 0.35 from laboratory experiments (Berni et al., 2017; Flores & Sleath, 1998) to 0.1 from the field experiment (Foster et al., 2006). The Sleath parameter associated with the high intensity and skewness wave condition (I85B78) is $S = 0.2$. Simulation results suggested that plug flow formation also depends on the sediment bed characteristics due to different size distributions as the plug flow did not occur for the WS-M and WS-C distributions. This finding motivates further research need on incorporating the effect of vertical sorting on generation of plug flow in the parameterized methods (e.g., Sleath parameter).

5. Discussion

5.1. Parameterization of Sheet Flow Layer Thickness

Unsteady effects such as the phase lags in sediment entrainment and suspension and plug flow under rapid flow acceleration have been the focus of high resolution measurements of intra-wave sediment fluxes (Mieras et al., 2019) and empirical parameterizations (Van der A et al., 2013). However, similar studies have yet to include size gradation effects on wave-driven sediment transport. The discussion focuses on investigating size gradation effects on the parameterization of sheet flow layer thickness.

Figure 8 shows the dimensionless sheet flow layer thickness ($Y = \delta_{s,max} / d_{50}$) as a function of maximum Shields number (θ_{max}) for the three sediment size distributions (Table 2) under the simulated eight wave conditions (Table 3). The sheet flow layer thickness was defined as the thickness of the sediment layer between volumetric concentrations of 0.60 (erosion depth) and 0.08 (sediment suspension threshold) (e.g., O'Donoghue & Wright, 2004a). For the BM distribution, since the bed surface was dominated by the coarse fraction, the dimensionless sheet flow layer thickness was calculated using the coarse fraction median diameter ($d_{50,c} = 0.97$ mm).

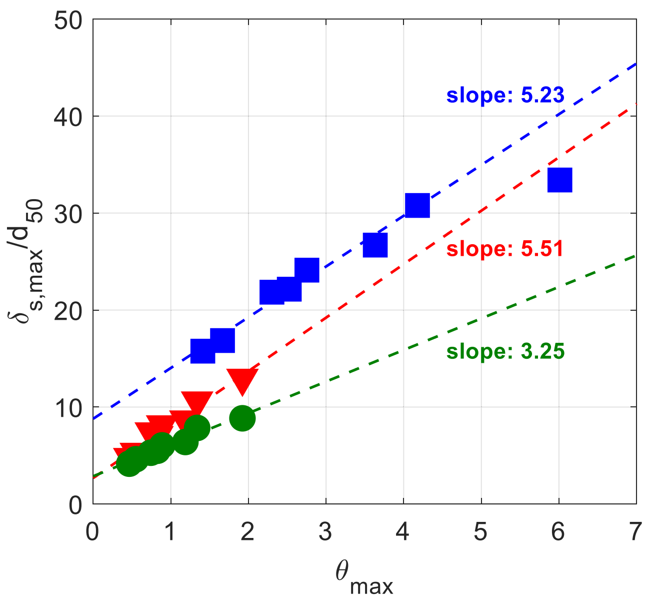

Figure 8. Sheet flow layer thickness, normalized by median grain size is plotted as a function of the maximum Shields parameter for WS-M (blue), WS-C (red), and BM (green) distributions with least square best fits shown (dashed lines). For WS-M the value of $\theta_{max} = 6.01$ (flow I85B78, Table 3) has been excluded from the least square fit.

Similar to previous studies (Dong et al., 2013; Mieras et al., 2017; Ribberink et al., 2008), $Y = \delta_{s,max}/d_{50}$ followed almost linearly a function of θ_{max} for different sediment size distributions. For the WS-M distribution, Y was higher than those of WS-C and BM under the same flow conditions, suggesting that the normalized sheet flow layer thickness may further depend on the grain size (or the fall parameter defined as the ratio of settling velocity to friction velocity). The normalized sheet flow layer thickness Y of WS-M under the highest wave intensity and skewness (I85B78, $\theta_{max} = 6.01$) deviates from the linear trend (the linear trend is observed up to $\theta_{max} = 4.18$). The observed deviation was due to the delayed entrainment and phase lags in particle settling of WS-M under the high intensity and high skewness wave condition (I85B78) discussed in Section 4.3; it is consistent with the observation that sediment fluxes of WS-M were below those of WS-C and BM near the peak crest (Figure 4f). Therefore, the fitted line for WS-M series excluded the high intensity and skewness case (I85B78). For the BM distribution, the maximum sheet flow layer thickness values followed that of WS-C for $\theta_{max} < 0.89$. At higher θ_{max}, the sheet flow layer thickness for the BM and WS-C distributions started deviating although for both cases the bed surface layer was composed of similar coarse sand particles (Figure 7c, $z \sim 0$). In particular, under the wave with the highest intensity and skewness (I85B78, $\theta_{max} = 1.92$), Y of the BM was reduced to 32% lower than that of the WS-C, which can be attributed to the formation of the high mobility coarse sand transport layer over the relatively smooth finer sand layer below (Figure 7c). As the waves were less energetic (smaller values of θ_{max}) the flow field can entrain mainly the coarse particles abundant on the surface layer of the BM, which is similar to the particles on the surface layer of WS-C (Figure 7c, $z \sim 0$). However, for high energy waves (higher values of θ_{max}), the flow field may be able to entrain more layers of sediment and hence the finer particles below the surface layer of the BM may become mobilized (Figure 7c, $z < 0$). Accordingly, values of Y for the BM calculated based on d_{50} of the coarse fraction (0.97 mm) had lower values compared to those of WS-C for high-energy waves. Interestingly, the slopes of the fitted lines for the WS-M and WS-C distributions were similar and remarkably higher than that of the BM distribution, confirming the unique feature of entrainment and transport associated with the bimodal sediment bed.

Lanckriet and Puleo (2015) developed a semi-analytical approach to quantify the intra-wave sheet flow layer thickness based on a force balance between shear stress, granular friction, and pressure gradient. Accordingly, the following equation was proposed to estimate the dimensionless sheet flow layer thickness (δ_s) for flow tunnel data,

$$C_1 \frac{w}{g} \frac{dY}{dt} = -Y \left(0.425 c_0 C_2 tan(\phi) - S \frac{U_0}{|U_0|} \right) + \theta \frac{U_0}{|U_0|} \tag{6}$$

where $c_0 = 0.6$ is the concentration at the bottom of sheet flow layer. C_1 and C_2 are dimensionless coefficients to parameterize the phase lag of the sheet flow layer and uncertainties in granular friction, respectively. In derivation of (6) the concentration profile within the sheet flow layer was obtained using the equation by O'Donoghue and Wright (2004a). The only unknown term in (6) is the bed shear stress θ, which is obtained using the boundary layer momentum integral method (see Appendix A). For the calculation of the BM distribution, the median grain diameter of the coarse fraction ($d_{50,c}$) was again used due to the predominance of coarse fraction in the surface layer. The maximum Shields parameter calculated by the momentum integral method were compared with those reported in Table 4 calculated using Soulsby (1997) (Figure 9). The values calculated using the two approaches show good agreement for different sediment size distributions lying along the perfect agreement line.

Using the simulation results, the coefficient C_1 in (6), which parameterizes the phase lags in the sheet flow layer was calibrated (see Table 6) by minimizing the root-mean-square-error (RMSE) between the peak sheet flow layer thickness obtained from the present model results $\delta_{s,max,CFDEM}$ and the ones calculated using the semi-analytical formulation $\delta_{s,max,LP}$. Here, the coefficient C_2 related to the granular friction was kept the same as

Version of record at: https://doi.org/10.1029/2022JC018686

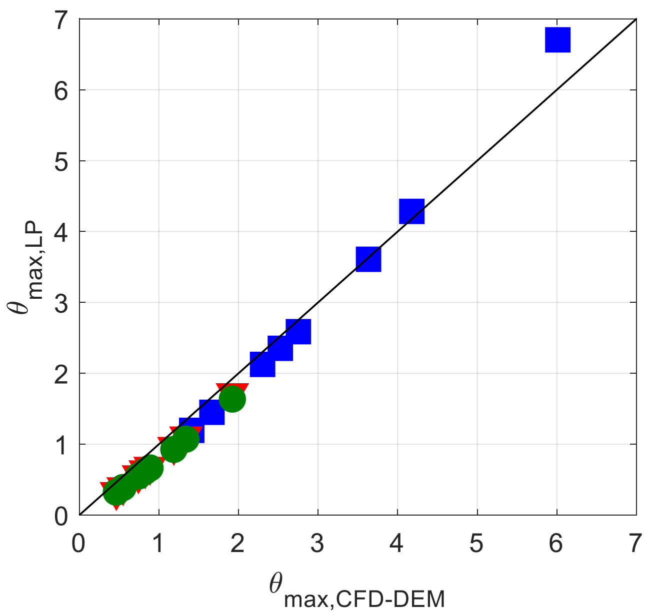

Figure 9. Comparison of maximum Shields parameter predicted by the semi-analytical model of Lanckriet and Puleo (2015) (LP) with the ones calculated from Soulsby (1997). One-to-one correspondence is shown by the black line.

the value calibrated by Lanckriet and Puleo (2015) for the tunnel flow experiments as $C_2 = 0.57$. Figure 10 shows the scatter plots of the maximum sheet flow layer thickness values obtained from the semi-analytical model using calibrated C_1 for each size distribution compared with the simulation results. A good agreement between the simulation results and semi-analytical model results where the differences between the values are smaller than 50%. Based on present simulation results, the coefficient C_1 was found to be dependent on the sediment size distribution. For WS-C and WS-M distributions values of C_1 were obtained as 15 and 88, respectively. The implication is that phase lag effects were more pronounced for WS-M distribution, consistent with results presented in Section 4.3. Interestingly, for the BM distribution $C_1 = 19$ was obtained, which shows that the response of the bimodal distribution having only 30% of coarse fraction was more similar to that of the WS-C distribution, consistent with the results presented in the previous sections.

5.2. Uncertainty in Morphodynamic Modeling

Most of regional-scale morphodynamic models assume a bed sediment consisting of uniform-sized particles in calculations of wave-averaged sediment transport rates. However, analysis from the present study suggests that wave-induced sediment transport is highly sensitive to the sediment size distribution. Specifically, phase lags in particle entrainment and particle settling intervals and generation of plug flow under high energy waves (commonplace during storm conditions) were found to be highly dependent on the bed sediment being of well-sorted or mixed size distributions, which can enhance or reduce the net transport rates by about 50%. The uncertainty in sediment size distribution in the regional-scale morphodynamic modeling may be part of the reason why the calibration of hydrodynamic and morphodynamic parameters were found to be site-specific and event specific (Rafati et al., 2021; Simmons et al., 2019). Current challenges in morphodynamic modeling of non-uniform bed sediment include the scarcity of measured data on sediment size characteristics in specific sites, efficiency of existing morphodynamic models to simulate spatial variation of sediment sizes due to vertical and horizontal sediment size sorting, and the skill of available practical methods in parameterizing the effect of sediment size gradation (Sherwood et al., 2021). Inclusion of the effect of sediment size distribution may increase the skill of nearshore models in predicting beach erosion and recovery during and after extreme events and may lower the dependency of the calibration parameters to specific sites or events.

6. Conclusions

Extensive Eulerian-Lagrangian simulations of sediment beds composed of well-sorted coarse sand ($d_{50} = 0.97$ mm), well-sorted medium sand ($d_{50} = 0.21$ mm), and mixed sand with a bimodal distribution consisting of 70% medium sand and 30% coarse sand were performed under a variety of oscillatory flow conditions to study how the vertical sorting affects the wave-driven sediment entrainment and transport. It was found that the response of the mixed sand to the oscillatory wave motion is similar to the response of the well-sorted coarse sand due to the abundance of the coarse fraction on the bed surface layer of the mixed sand. Furthermore, inverse grading (upward coarsening) formed for the sediment bed of mixed sand caused higher sediment fluxes due to the medium fraction underneath the surface layer of coarse fraction facilitating the sediment pickup. Under the high wave intensity and skewness condition, the unique sorting feature further caused the generation of plug flow for the mixed sand not observed for the well-sorted sands. For the well-sorted medium sand under high wave skewness and intensity, phase-lags in particle entrainment were present, which was caused by relatively short crest interval and relatively high crest velocity amplitude where the medium sand particles

Table 6
Calibrated Coefficients of Lanckriet and Puleo (2015) Semi-Analytical Model

Distribution	Category	C_1	C_2
WS-M	well-sorted medium	88	0.57
WS-C	well-sorted coarse	15	0.57
BM*	bimodal	19	0.57

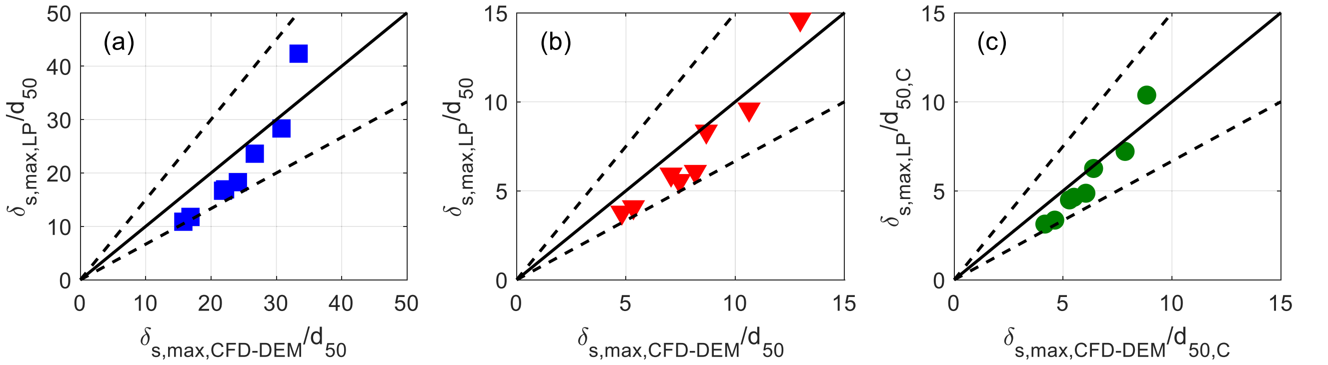

Figure 10. Maximum sheet flow layer thickness predicted by the calibrated semi-analytical model of Lanckriet and Puleo (2015) (LP) versus those calculated from the present simulations (CFD-DEM) for WS-M (a), WS-C (b), and BM (c) size distributions. One-to-one correspondence is shown by the solid-black lines and the dashed-black lines have slopes 3/2 and 2/3.

do not have enough time to become entrained. For the well-sorted coarse sand, the bedload transport was dominant during the crest interval, which caused faster settling of the particles after the peak flow crest.

Overall, it was found that sediment size distribution can enhance or reduce the net sediment transport rates by about 50%, which may be part of the uncertainty in existing morphodynamic models. Therefore, incorporating the effect of sediment size distribution in sediment transport parameterizations in regional-scale morphodynamic modeling may lower the dependency of calibration coefficients to specific sites and events. A semi-analytical method of quantifying the sheet flow layer thickness under wave motion was tested and calibrated for the present simulation results of different bed sediment configurations. The calibration results were also consistent with the analysis of the model results confirming that the sediment transport of the mixed sand is dominated by the coarse fraction and the phase lags were more effective for well-sorted medium sand.

Appendix A: Lanckriet and Puleo (2015) Parameterization Details

To obtain the bed shear stress in Equation 6 the boundary layer integral method is used (Fredsoe, 1984),

$$\frac{dZ}{dt} = \left(\frac{k^2 U}{z_0} - Z\left(e^Z - Z - 1\right)\frac{1}{U}\frac{dU}{dt} - \frac{e^Z - 1}{z_0}\frac{dz_0}{dt}\right) / \left(e^Z (Z - 1) + 1\right) \tag{A1}$$

where the dimensionless parameter Z is defined as,

$$Z(t) = \frac{U(t)}{U_*(t)}\kappa, \tag{A2}$$

where κ is the von Karman constant set to 0.41, $U_*(t) = \sqrt{\tau/\rho} sign(U)$ is the friction velocity. Assuming log-law velocity profile in the wave boundary layer, Z at the top of the wave boundary layer ($z = \delta_b$) is written as,

$$Z = ln\left(\frac{\delta_b + z_0}{z_0}\right), \tag{A3}$$

where $z_0 = K_n/30$, K_n is the bed roughness calculated based on the bed grain size and sheet flow layer thickness as,

$$K_N = 2.5 d_{50} + 0.5\delta_s. \tag{A4}$$

Equations 6 and A1 were solved simultaneously using MATLAB ODE solver "ode15s" based on iteration to the point the difference between successive sheet layer thickness values converge to smaller than 10^{-6} m.

Data Availability Statement

The source code and model setup of validation and simulation cases are available through GitHub: https://github.com/Yashar-Rafati/CFD-DEM (source code); https://github.com/Yashar-Rafati/CFD-DEM-Validation (model setup for validation cases); https://github.com/Yashar-Rafati/CFD-DEM-Simulation (model setup for simulations).

Acknowledgments
This study was supported by Office of Naval Research (N00014-18-1-2785) and National Science Foundation (OCE-1756714). Joseph Calantoni was supported under base funding to the U.S. Naval Research Laboratory from the Office of Naval Research. Numerical simulations presented in this study were carried out using the Caviness cluster at University of Delaware, and the Expanse cluster at San Diego Supercomputer Center via XSEDE.

References

Abreu, T., Silva, P. A., Sancho, F., & Temperville, A. (2010). Analytical approximate wave form for asymmetric waves. *Coastal Engineering*, *57*(7), 656–667. https://doi.org/10.1016/j.coastaleng.2010.02.005

Ahmed, A. S. M., & Sato, S. (2003a). A sheetflow transport model for asymmetric oscillatory flows, Part I: Uniform grain size sediments. *Coastal Engineering Journal*, *45*(3), 321–337. https://doi.org/10.1142/S0578563403000786

Ahmed, A. S. M., & Sato, S. (2003b). A sheetflow transport model for asymmetric oscillatory flows, part II: Mixed grain size sediments. *Coastal Engineering*, *45*(3), 339–361. https://doi.org/10.1142/S0578563403000798

Anderson, D., Cox, D. T., Mieras, R. S., Puleo, J. A., & Hsu, T.-J. (2017). Observations of wave-induced pore pressure gradients and bed level response on a surf zone sandbar. *Journal of Geophysical Research: Oceans*, *122*(6), 5169–5193. https://doi.org/10.1002/2016JC012557

Balachandar, S., & Eaton, J. K. (2010). Turbulent dispersed multiphase flow. *Annual Review of Fluid Mechanics*, *42*(1), 111–133. https://doi.org/10.1146/annurev.fluid.010908.165243

Berni, C., Michallet, H., & Barthélemy, E. (2017). Effects of horizontal pressure gradients on bed destabilization under waves. *Journal of Fluid Mechanics*, *812*, 721–751. https://doi.org/10.1017/jfm.2016.805

Brinkkemper, J. A., Aagaard, T., Bakker, A. T. M., & Ruessink, B. G. (2018). Shortwave sand transport in the shallow surf zone. *Journal of Geophysical Research: Earth Surface*, *123*(5), 1145–1159. https://doi.org/10.1029/2017JF004425

Calantoni, J., & Puleo, J. A. (2006). Role of pressure gradients in sheet flow of coarse sediments under sawtooth waves. *Journal of Geophysical Research*, *111*(C1), C01010. https://doi.org/10.1029/2005JC002875

Calantoni, J., & Thaxton, C. S. (2008). Simple power law for transport ratio with bimodal distributions of coarse sediments under waves. *Journal of Geophysical Research*, *113*(C3), C03003. https://doi.org/10.1029/2007JC004237

Cheng, Z., Chauchat, J., Hsu, T. J., & Calantoni, J. (2018). Eddy interaction model for turbulent suspension in Reynolds-averaged Euler–Lagrange simulations of steady sheet flow. *Advances in Water Resources*, *111*, 435–451. https://doi.org/10.1016/j.advwatres.2017.11.019

Cheng, Z., Hsu, T. J., & Calantoni, J. (2017). SedFoam: A multi-dimensional Eulerian two-phase model for sediment transport and its application to momentary bed failure. *Coastal Engineering*, *119*, 32–50. https://doi.org/10.1016/j.coastaleng.2016.08.007

Cundall, P. A., & Strack, O. D. L. (1979). A discrete numerical model for granular assemblies. *Géotechnique*, *29*(1), 47–65. https://doi.org/10.1680/geot.1979.29.1.47

Dibajnia, M., & Watanabe, A. (1996). A transport rate formula for mixed-size sands. *Coastal Engineering Proceedings*, 3791–3804. https://doi.org/10.1061/9780784402429.293

Dohmen-Janssen, C. M., Kroekenstoel, D. F., Hassan, W. N., & Ribberink, J. S. (2002). Phase lags in oscillatory sheet flow: Experiments and bed load modelling. *Coastal Engineering*, *46*(1), 61–87. https://doi.org/10.1016/S0378-3839(02)00056-X

Dohmen-Janssen, M. (1999). Grain size influence on sediment transport in oscillatory sheet flow: Phase lags and mobile-bed effects. In *PhD Thesis*. Delft University of Technology. Retrieved from https://repository.tudelft.nl/islandora/object/uuid%3Ab448c04e-914c-484c-94cb-bcf046f6609f

Dong, L. P., Sato, S., & Liu, H. (2013). A sheetflow sediment transport model for skewed-asymmetric waves combined with strong opposite currents. *Coastal Engineering*, *71*, 87–101. https://doi.org/10.1016/j.coastaleng.2012.08.004

Drake, G., & Calantoni, J. (2001). Discrete particle model for sheet flow sediment transport in the nearshore. *Journal of Geophysical Research*, *106*(C9), 19859–19868. https://doi.org/10.1029/2000JC000611

Elgar, S., Gallagher, E. L., & Guza, R. T. (2001). Nearshore sandbar migration. *Journal of Geophysical Research*, *106*(C6), 11623–11627. https://doi.org/10.1029/2000JC000389

Elgar, S., Guza, R. T., & Freilich, M. H. (1988). Eulerian measurements of horizontal accelerations in shoaling gravity waves. *Journal of Geophysical Research*, *93*(C8), 9261–9269. https://doi.org/10.1029/JC093iC08p09261

Finn, J. R., Li, M., & Apte, S. V. (2016). Particle based modelling and simulation of natural sand dynamics in the wave bottom boundary layer. *Journal of Fluid Mechanics*, *796*, 340–385. https://doi.org/10.1017/jfm.2016.246

Flores, N. Z., & Sleath, J. F. A. (1998). Mobile layer in oscillatory sheet flow. *Journal of Geophysical Research*, *103*(C6), 12783–12793. https://doi.org/10.1029/98JC00691

Foster, D. L., Bowen, A. J., Holman, R. A., & Natoo, P. (2006). Field evidence of pressure gradient induced incipient motion. *Journal of Geophysical Research*, *111*, C05004. https://doi.org/10.1029/2004JC002863

Fredsoe, J. (1984). Turbulent boundary layer in wave-current motion. *Journal of Hydraulic Engineering*, *110*(8), 1103–1120. https://doi.org/10.1061/(ASCE)0733-9429

Gallagher, E. L., Elgar, S., & Guza, R. T. (1998). Observations of sand bar evolution on a natural beach. *Journal of Geophysical Research*, *103*(C2), 3203–3215. https://doi.org/10.1029/97JC02765

Goniva, C., Kloss, C., Deen, N. G., Kuipers, J. A. M., & Pirker, S. (2012). Influence of rolling friction on single spout fluidized bed simulation. *Particuology*, *10*(5), 582–591. https://doi.org/10.1016/j.partic.2012.05.002

Graham, D. I., & James, P. W. (1996). Turbulent dispersion of particles using eddy interaction models. *International Journal of Multiphase Flow*, *22*(1), 157–175. https://doi.org/10.1016/0301-9322(95)00061-5

Harada, E., & Gotoh, H. (2008). Computational mechanics of vertical sorting of sediment in sheetflow regime by 3D granular material model. *Coastal Engineering Journal*, *50*(1), 19–45. https://doi.org/10.1142/S0578563408001715

Hassan, W. N., & Ribberink, J. S. (2005). Transport processes of uniform and mixed sands in oscillatory sheet flow. *Coastal Engineering*, *52*(9), 745–770. https://doi.org/10.1016/j.coastaleng.2005.06.002

Hegermiller, C. A., Warner, J. C., Olabarrieta, M., Sherwood, C. R., & Kalra, T. S. (2022). Modeling of barrier breaching during Hurricanes sandy and Matthew. *Journal of Geophysical Research: Earth Surface*, *127*(3). https://doi.org/10.1029/2021jf006307

Holland, K. T., & Elmore, P. A. (2008). A review of heterogeneous sediments in coastal environments. *Earth-Science Reviews*, *89*(3–4), 116–134. https://doi.org/10.1016/j.earscirev.2008.03.003

Huisman, B. J. A., Schipper, M. A., & Ruessink, B. G. (2016). Sediment sorting at the Sand Motor at storm and annual time scales. *Marine Geology*, *381*, 209–226. https://doi.org/10.1016/j.margeo.2016.09.005

Kaczmarek, L. M., Biegowski, J., & Ostrowski, R. (2004). Modelling cross-shore intensive sand transport and changes of bed grain size distribution versus field data. *Coastal Engineering*, *51*(5–6), 501–529. https://doi.org/10.1016/j.coastaleng.2004.05.007

Kalra, T. S., Sherwood, C. R., Warner, J. C., Rafati, Y., & Hsu, T.-J. (2019). Investigating bedload transport under asymmetrical waves using a coupled Ocean-wave model. *Coastal Sediments*. https://doi.org/10.1142/9789811204487_0052

Kloss, C., Goniva, C., Hager, A., Amberger, S., & Pirker, S. (2012). Models, algorithms and validation for opensource DEM and CFD-DEM. *Progress in Computational Fluid Dynamics*, *12*(2–3), 140–152. https://doi.org/10.1504/PCFD.2012.047457

Lanckriet, T., & Puleo, J. A. (2015). A semianalytical model for sheet flow layer thickness with application to the swash zone. *Journal of Geophysical Research: Oceans*, *120*(2), 1333–1352. https://doi.org/10.1002/2014JC010378

Liu, H., & Sato, S. (2005). Laboratory study on sheetflow sediment movement in the oscillatory turbulent boundary layer based on image analysis. *Coastal Engineering Journal*, *47*(1), 21–40. https://doi.org/10.1142/S057856340500115X

Luding, S. (2008). Introduction to discrete element methods: Basic of contact force models and how to perform the micro-macro transition to continuum theory. *European Journal of Environmental and Civil Engineering*, *12*(7–8), 785–826. https://doi.org/10.1080/19648189.2008.9693050

Mieras, R. S., Puleo, J. A., Anderson, D., Cox, D. T., & Hsu, T.-J. (2017). Large-scale experimental observations of sheet flow on a sandbar under skewed-asymmetric waves. *Journal of Geophysical Research: Oceans*, *122*(6), 5022–5045. https://doi.org/10.1002/2016JC012438

Mieras, R. S., Puleo, J. A., Anderson, D., Hsu, T.-J., Cox, D. T., & Calantoni, J. (2019). Relative contributions of bed load and suspended load to sediment transport under skewed-asymmetric waves on a sandbar crest. *Journal of Geophysical Research: Oceans*, *124*(2), 1294–1321. https://doi.org/10.1029/2018jc014564

Nielsen, P. (1983). Entrainment and distribution of different sand sizes under water waves. *Journal of Sedimentary Petrology*, *53*(2), 423–428. https://doi.org/10.1306/212F81F7-2B24-11D7-8648000102C1865D

Nielsen, P. (2006). Sheet flow sediment transport under waves with acceleration skewness and boundary layer streaming. *Coastal Engineering*, *53*(9), 749–758. https://doi.org/10.1016/j.coastaleng.2006.03.006

O'Donoghue, T., & Wright, S. (2004a). Concentrations in oscillatory sheet flow for well sorted and graded sands. *Coastal Engineering*, *50*(3), 117–138. https://doi.org/10.1016/j.coastaleng.2003.09.004

O'Donoghue, T., & Wright, S. (2004b). Flow tunnel measurements of velocities and sand flux in oscillatory sheet flow for well-sorted and graded sands. *Coastal Engineering*, *51*(11–12), 1163–1184. https://doi.org/10.1016/j.coastaleng.2004.08.001

Pender, D., & Karunarathna, H. (2013). A statistical-process based approach for modelling beach profile variability. *Coastal Engineering*, *81*, 19–29. https://doi.org/10.1016/j.coastaleng.2013.06.006

Prodger, S., Russell, P., Davidson, M., Miles, J., & Scott, T. (2016). Understanding and predicting the temporal variability of sediment grain size characteristics on high-energy beaches. *Marine Geology*, *376*, 109–117. https://doi.org/10.1016/j.margeo.2016.04.003

Rafati, Y., Hsu, T., Elgar, S., Raubenheimer, B., Quataert, E., & Van Dongeren, A. (2021). Modeling the hydrodynamics and morphodynamics of sandbar migration events. *Coastal Engineering*, *166*, 103885. https://doi.org/10.1016/j.coastaleng.2021.103885

Rafati, Y., Hsu, T.-J., Cheng, Z., Yu, X., & Calantoni, J. (2020). Armoring and exposure effects on the wave-driven sediment transport. *Continental Shelf Research*, *211*, 104291. https://doi.org/10.1016/j.csr.2020.104291

Ribberink, J. S., & Al-Salem, A. A. (1994). Sediment transport in oscillatory boundary layers in cases of rippled beds and sheet flow. *Journal of Geophysical Research*, *99*(C6), 12707–12727. https://doi.org/10.1029/94JC00380

Ribberink, J. S., vanderWerf, J. J., O'Donoghue, T., & Hassan, W. N. M. (2008). Sand motion induced by oscillatory flows: Sheet flow and vortex ripples. *Journal of Turbulence*, *9*(20), 1–32. https://doi.org/10.1080/14685240802220009

Ruessink, B. G., Blenkinsopp, C., Brinkkemper, J. A., Castelle, B., Dubarbier, B., Grasso, F., et al. (2016). Sandbar and beach-face evolution on a prototype coarse sandy barrier. *Coastal Engineering*, *113*, 19–32. https://doi.org/10.1016/j.coastaleng.2015.11.005

Ruessink, B. G., Michallet, H., Abreu, T., Sancho, F., Van Der A, D. A., Van Der Werf, J. J., & Silva, P. A. (2011). Observations of velocities, sand concentrations, and fluxes under velocity-asymmetric oscillatory flows. *Journal of Geophysical Research*, *116*(C3), C03004. https://doi.org/10.1029/2010JC006443

Ruessink, B. G., Ramaekers, G., & Van Rijn, L. C. (2012). On the parameterization of the free-stream non-linear wave orbital motion in nearshore morphodynamic models. *Coastal Engineering*, *65*, 56–63. https://doi.org/10.1016/j.coastaleng.2012.03.006

Schmeeckle, M. W., Nelson, J. M., Pitlick, J., & Bennett, J. P. (2001). Interparticle collision of natural sediment grains in water. *Water Resources Research*, *37*(9), 2377–2391. https://doi.org/10.1029/2001WR000531

Schretlen, J. L. M. (2012). Sand transport under full-scale progressive surface waves. In *PhD Thesis*. University of Twente. Retrieved from https://research.utwente.nl/en/publications/sand-transport-under-full-scale-progressive-surface-waves

Schwartz, R. K., & Birkemeier, W. A. (2004). Sedimentology and morphodynamics of a barrier island shoreface related to engineering concerns, Outer Banks, NC, USA. *Marine Geology*, *211*(3–4), 215–255. https://doi.org/10.1016/j.margeo.2004.05.020

Sherwood, C. R., Van Dongeren, A. R., Doyle, J., Hegermiller, C. A., Hsu, T. J., Kalra, T. S., et al. (2021). Modeling morphodynamics of coastal response to extreme events: What shape are we in? *Annual Review of Marine Science*, *14*(1), 457–492. https://doi.org/10.1146/annurev-marine-032221-090215

Shimamoto, T. (2016). *Beach recovery and studies in accretive sediment transport. PhD Thesis*. The University of Queensland. Retrieved from https://espace.library.uq.edu.au/view/UQ:387531

Simmons, J. A., Splinter, K. D., Harley, M. D., & Turner, I. L. (2019). Calibration data requirements for modelling subaerial beach storm erosion. *Coastal Engineering*, *152*, 103507. https://doi.org/10.1016/j.coastaleng.2019.103507

Sleath, J. F. A. (1999). Conditions for plug formation in oscillatory flow. *Continental Shelf Research*, *19*(13), 1643–1664. https://doi.org/10.1016/S0278-4343(98)00096-X

Soulsby, R. L. (1997). *Dynamics of Marine Sands*. Thomas Telford Publications.

Stauble, D. (1992). *Long-term profile and sediment morphodynamics: Field Research Facility case history. Technical Report CERC-92-7*. U.S Army Corps of Engineers. Retrieved from https://apps.dtic.mil/sti/citations/ADA255284

Van der A, D. A., O'Donoghue, T., & Ribberink, J. S. (2010). Measurements of sheet flow transport in acceleration-skewed oscillatory flow and comparison with practical formulations. *Coastal Engineering*, *57*(3), 331–342. https://doi.org/10.1016/j.coastaleng.2009.11.006

Van der A, D. A., Ribberink, J. S., Van der Werf, J. J., O'Donoghue, T., Buijsrogge, R. H., & Kranenburg, W. M. (2013). Practical sand transport formula for non-breaking waves and currents. *Coastal Engineering*, *76*, 26–42. https://doi.org/10.1016/j.coastaleng.2013.01.007

Van der Lugt, M. A., Quataert, E., Van Dongeren, A., Van Ormondt, M., & Sherwood, C. R. (2019). Morphodynamic modeling of the response of two barrier islands to Atlantic hurricane forcing. *Estuarine, Coastal and Shelf Science*, *229*, 106404. https://doi.org/10.1016/j.ecss.2019.106404

Van der Zanden, J., vanDer, A. D. A., Hurther, D., Caceres, I., O'Donoghue, T., Hulscher, S. J. M. H., & Ribberink, J. S. (2017). Bedload and suspended load contributions to breaker bar morphodynamics. *Coastal Engineering*, *129*, 74–92. https://doi.org/10.1016/j.coastaleng.2017.09.005

Van der Zanden, J., Van Der A, D. A., Hurther, D., Caceres, I., O'Donoghue, T., & Ribberink, J. S. (2016). Near-bed hydrodynamics and turbulence below a large-scale plunging breaking wave over a mobile barred bed profile. *Journal of Geophysical Research: Oceans*, *121*(8), 6482–6506. https://doi.org/10.1002/2016JC011909

Van Rijn, L. C. (2007a). Unified view of sediment transport by currents and waves. I: Initiation of motion, bed roughness, and bed-load transport. *Journal of Hydraulic Engineering*, *133*(6), 649–667. https://doi.org/10.1061/(asce)0733-9429(2007)133:6(649)

Van Rijn, L. C. (2007b). Unified view of sediment transport by currents and waves. II: Suspended transport. *Journal of Hydraulic Engineering*, *133*(6), 668–689. https://doi.org/10.1061/(asce)0733-9429(2007)133:6(668)

Watanabe, A., & Sato, S. (2004). A sheet-flow transport rate formula for asymetric, forward-leaning waves and currents. *Coastal Engineering Proceedings*, 1703–1714. https://doi.org/10.1142/9789812701916_0136

Wiberg, P. L., Drake, D. E., & Cacchione, D. A. (1994). Sediment resuspension and bed armoring during high bottom stress events on the northern California inner continental shelf: Measurements and predictions. *Continental Shelf Research*, *14*(10–11), 1191–1219. https://doi.org/10.1016/0278-4343(94)90034-5